VCU

VIRGINIA COMMONWEALTH UNIVERSITY

Virginia Commonwealth University
VCU Scholars Compass

Electrical and Computer Engineering Publications | Dept. of Electrical and Computer Engineering

2008

Optical transitions in a quantum wire with spin-orbit interaction and its applications in terahertz electronics: Beyond zeroth-order theory

P. Upadhyaya
Indian Institute of Technology

S. Pramanik
Virginia Commonwealth University

S. Bandyopadhyay
Virginia Commonwealth University, sbandy@vcu.edu

Optical transitions in a quantum wire with spin-orbit interaction and its applications in terahertz electronics: Beyond zeroth-order theory

P. Upadhyaya

Department of Electronics and Electrical Communications Engineering, Indian Institute of Technology, Kharagpur 721 302, India

S. Pramanik

Department of Electrical and Computer Engineering, University of Alberta, Edmonton, Alberta, Canada T6G 2V4

S. Bandyopadhyay

Department of Electrical and Computer Engineering, Virginia Commonwealth University, Richmond, Virginia 23284, USA

We calculate the terahertz absorption spectra associated with intersubband transitions in a semiconductor quantum wire in the presence of spin-orbit interaction and a transverse magnetic field. The frequencies and intensities of the absorption peaks are found to depend strongly on the spin-orbit coupling strength, which can be varied with an external electric field. This feature can be exploited to realize reconfigurable multispectral terahertz detectors and amplitude and/or frequency modulators. We also show that electric dipole transitions between spin-split levels in the same subband (which are normally deemed forbidden) become allowed because of spin texturing effects. The absorption associated with these transitions experience a redshift (blueshift) with increasing spin-orbit coupling strength for materials with negative (positive) *g* factor. The normally allowed transitions, on the other hand, experience the opposite shift, i.e., blue for materials with negative *g* factor and red for materials with positive *g* factor. The theory described here is universal and applies to all semiconductors.

I. INTRODUCTION

There is a great demand for terahertz modulators and multispectral detectors for communication, sensing, and signal processing applications. In this paper, we show that electrostatically modulated spin-orbit interaction in a quantum wire can be gainfully employed for this purpose. By varying the spin-orbit interaction strength in a quantum wire with an electric field, one can vary both the energy spacings between different subbands and the matrix element for radiative transitions between them. This allows one to modulate the frequency and amplitude of terahertz absorption and emission, thereby realizing "reconfigurable" multispectral terahertz detectors and amplitude and/or frequency modulators.

This paper is organized as follows. In Sec. II, we describe the theory used to calculate subband energy dispersion relations and the two-component spinor wave functions in a quantum wire subjected to a transverse magnetic field. Both Rashba[1] and Dresselhaus[2] spin-orbit interactions are assumed to be present in the wire and the former can be modulated with an externally applied electric field. This theory is then used in Sec. III to calculate the spatial modulation of the spin density across the width of the wire (in different subbands), the energy spacing between different subbands, and the matrix elements for photon induced transitions between them. We show that all of these quantities can be varied by varying the Rashba spin-orbit interaction strength with an external potential. Finally, in Sec. IV, we present the summary and conclusions.

II. THEORY

Consider a semiconductor quantum wire with rectangular cross section as shown in Fig. 1. We assume that the wire

material is InAs so that the effective mass of electrons is 0.03 times the free electron mass and the Landé *g* factor=−15. The axis of the wire is along $\hat{x}$, which coincides with the [100] crystallographic direction. A symmetry breaking transverse electric field $E_y\hat{y}$ induces Rashba spin-orbit coupling, whose strength can be varied by changing $E_y\hat{y}$ using a top gate terminal. InAs has a bulk inversion asymmetry in the microscopic crystal potential which induces the Dresselhaus spin-orbit coupling effect.[2] We also assume that there is an external magnetic field of flux density *B* along $\hat{y}$.

It has been pointed out[3,4] that if the nuclear spins in the quantum wire are polarized by some external means, such as optical pumping, then there will be an additional effective
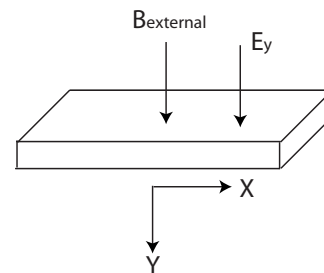
FIG. 1. A quantum wire of rectangular cross section with $W_y \ll W_z = 100$ nm. The wire axis ($\hat{x}$) is aligned along the [100] crystallographic direction. A top gate (not shown) applies a symmetry breaking electric field E_y along the *y* direction to induce the Rashba spin-orbit interaction in the wire. An external magnetic field *B* also acts along $\hat{y}$. For calculating intersubband transitions, we assume that the wire is irradiated by an electromagnetic wave [of frequency *f* (Hz)], which is linearly polarized along $\hat{z}$.

magnetic field arising from the nuclear spins, which can be quite strong. This field could result in time-dependent energy dispersion relations since the nuclear spins will precess about the external magnetic field. Under normal equilibrium conditions, the nuclear spins are depolarized and the effective magnetic field arising from them is negligible. Therefore, we can neglect such effects here since we do not consider a polarized background of nuclear spins.

In the Landau gauge $(Bz, 0, 0)$, the single particle effective mass Hamiltonian describing this system is

$$H = \frac{(\vec{p} + eBz\hat{x})^2}{2m^*} + V(y) + V(z) - \frac{g\mu_B \vec{B} \cdot \vec{\sigma}}{2} + \frac{\eta_R}{\hbar}[\sigma_z(p_x + eBz)$$

$$- \sigma_x p_z] + \frac{\eta_D}{\hbar} p_y^2 [\sigma_x(p_x + eBz) - \sigma_z p_z], \quad (1)$$

where g is the Landé g factor of the quantum wire material, η_R is the strength of the Rashba interaction (which depends on the top gate potential), and η_D is the strength of the Dresselhaus interaction. In writing the Dresselhaus term, we assumed that the thickness of the wire (along the $\hat{y}$ direction) is much smaller than the width (along the $\hat{z}$ direction). We also assume that η_R and η_D are spatially invariant within the wire.

Owing to the electric field E_y, the potential along $\hat{y}$ is given by $V(y) = -eE_y$. We assume that outside $[0, W_y]$, $V(y) \rightarrow \infty$. Similarly, in the $\hat{z}$ direction, we have $V(z) = 0$ for $0 \leq z \leq W_z$ and ∞ everywhere else.

We intend to calculate the energy eigenvalues (E) and the corresponding two-component spinor eigenfunctions (Ψ) of the Pauli equation $H\Psi = E\Psi$, where H is given by Eq. (1). Since the entire Hamiltonian H is translationally invariant along x and the coefficients of the Pauli matrices in H do not involve x and y coordinates, we can write $\Psi(x, y, z) = \exp(iq_x x)\varphi(y)[\zeta_\alpha(z)\zeta_\beta(z)]^T$, where the superscript T stands for transpose. Spatially averaging both sides of the Pauli equation over x and y coordinates yields,

$$E\zeta(z) = [H_0 I + H_s]\zeta(z), \quad (2a)$$

where I is the 2×2 identity matrix and

$$\zeta(z) = [\zeta_\alpha(z)\zeta_\beta(z)]^T, \quad (2b)$$

$$H_0 = \frac{\hbar^2 q_x^2}{2m^*} - \frac{\hbar^2}{2m^*}\frac{d^2}{dz^2} + \frac{eBz\hbar q_x}{m^*} + \frac{e^2 B^2 z^2}{2m^*} + \varepsilon_n + V(z),$$

$$(2c)$$

$$\left[-\frac{\hbar^2}{2m^*}\frac{d^2}{dy^2} + V(y)\right]\varphi_n(y) = \varepsilon_n \varphi_n(y), \quad (2d)$$

$$H_s = -\frac{g\mu_B B\sigma_y}{2} + \eta_R\left[\left(q_x + \frac{eBz}{\hbar}\right)\sigma_z + i\sigma_x\frac{d}{dz}\right]$$

$$+ \gamma_D\left[\left(q_x + \frac{eBz}{\hbar}\right)\sigma_x + i\sigma_z\frac{d}{dz}\right], \quad (2e)$$

and

$$\gamma_D = \eta_D \langle p_y^2 \rangle_n \equiv \eta_D \int_{-\infty}^{\infty} \varphi_n^*(y)\left[-\hbar^2\frac{d^2}{dy^2}\right]\varphi_n(y)dy. \quad (2f)$$

The quantity γ_D may be viewed as the *effective* Dresselhaus constant. Here, n indicates the subband index along the y direction and m along the z direction. We assume that W_y is sufficiently small so that only the lowest subband (in the y direction) is occupied by electrons, i.e., $n=1$, always. In the numerical results that will be presented later, the width along $\hat{z}$ (i.e., W_z) is assumed to have a fixed value of 100 nm. In order to calculate the energy dispersion $(E - q_x)$ relation of the magnetoelectric subbands in the wire and the two-component spinor wave function $\zeta(z)$, we solve the Pauli equation (2a) subject to the boundary conditions,

$$\zeta_\alpha(z = 0) = \zeta_\alpha(z = W_z) = 0,$$

$$\zeta_\beta(z = 0) = \zeta_\beta(z = W_z) = 0, \quad (3)$$

using a numerical recipe described elsewhere.[5]

III. RESULTS AND DISCUSSION

Figure 2(a) shows the typical energy dispersion relationship for $B = 1$ T in the presence of both Rashba and Dresselhaus spin-orbit interactions ($\eta_R = 3 \times 10^{-11}$ eV m and $\gamma_D = 1 \times 10^{-11}$ eV m). The horizontal axis represents the quantity $q_x + eBW_z/2\hbar$, which we refer to as the renormalized wave vector k_x in the rest of this paper. The symbols mL and mU ($m = 1, 2, 3, \ldots$), respectively, indicate the lower and upper spin-split levels of the mth subband. Note that for $B = 1$ T and $W_z = 100$ nm, the electronic states can be broadly classified as either edge states or bulk states (also known as two-dimensional states or Landau orbit states). The bulk states have small k_x and execute cyclotron motion in closed Landau orbits at or near the center of the wire, while the edge states have larger k_x, are localized near the edges of the wire, and correspond to skipping orbits.[6,7] Figure 2(b) shows the real and imaginary parts of the bulk state two-component wave function $[\zeta_\alpha(z)\zeta_\beta(z)]^T$ (at $k_x = 0$) of $1L$ subband. As expected, these wave functions are localized (peaked) near the center of the wire.

It should be emphasized that in the presence of spin-orbit interaction, it is not possible to separate the spatial and spin part of the spinor wave function. In other words, one cannot write $[\zeta_\alpha(z, k_x, m_\mp) \ \zeta_\beta(z, k_x, m_\mp)]^T = \psi(z, k_x, m)[\alpha_0(k_x, \mp)\beta_0(k_x, \mp)]^T$, where α_0 and β_0 are z independent and $\mp$ stands for the L (upper sign) and U (lower sign) spin-split levels in any subband m. It is customary to separate the spatial and spin parts in the above fashion in zeroth-order theory, which, as a consequence, misses many important features that we discussed in [8] and will discuss more in this paper. In fact, zeroth-order theory will miss all of spin texturing effects[8,9] and *incorrectly* conclude that electric dipole transitions between spin-split levels of the same subband are forbidden, when they are not. We will explicitly show that later.
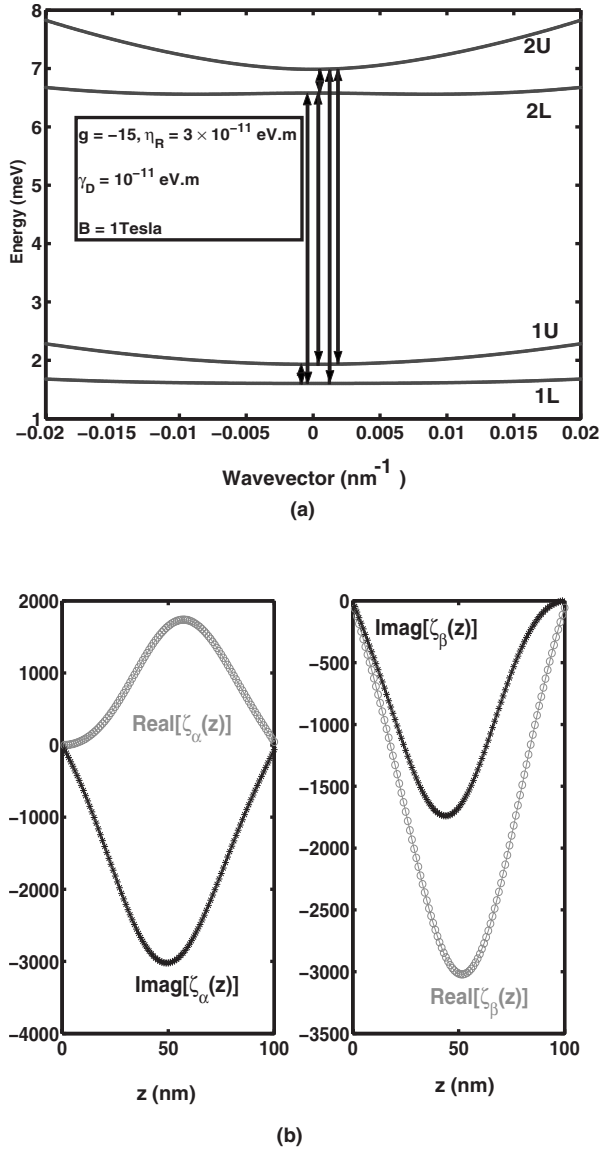
FIG. 2. (a) $E-k_x$ plot for $B=1$ T, η_R (Rashba coupling strength) $=3\times10^{-11}$ eV m, and γ_D (Dresselhaus coupling strength) $=1\times10^{-11}$ eV m. The material parameters of InAs have been used ($m^*=0.03\,m_0$ and $g=-15$). The label $mL(mU)$ indicates lower (upper) spin-split level of subband $m=1,2,3,\ldots$. The vertical arrows denote the photon induced transitions between $1L$ and other energy levels that were considered in this paper. (b) The two-component spinor wave function $\zeta(z,k_x,m_\mp)=[\zeta_\alpha(z,k_x,m_\mp)\,\zeta_\beta(z,k_x,m_\mp)]^T$ as a function of the position z along the width of the wire. These wave functions are for the $1L$ level at $k_x=0$. The external magnetic field strength and the spin-orbit interaction strengths are the same as in (a).

We define spin components S_j as

$$\Sigma_j(z,k_x,m_\mp)=[\zeta_\alpha^*(z,k_x,m_\mp)\zeta_\beta^*(z,k_x,m_\mp)]\sigma_j[\zeta_\alpha(z,k_x,m_\mp)$$

$$\times\zeta_\beta(z,k_x,m_\mp)]^T, \quad j=x,y,z,$$

$$S_j(z,k_x,m_\mp)=\frac{\Sigma_j(z,k_x,m_\mp)}{\sqrt{\Sigma_x^2(z,k_x,m_\mp)+\Sigma_y^2(z,k_x,m_\mp)+\Sigma_z^2(z,k_x,m_\mp)}}.$$

(4)

These quantities not only depend on k_x and the level index ($mL/U=m_\mp$) but depend on z as well. Therefore, an electron, with fixed k_x and belonging to a particular energy level (mL/U), has different spin orientations depending on its physical location along the width of the quantum wire channel. As a result, the spin density varies along z. This effect is known as "spin texturing."[8,9]

In order to study the effect of spin-orbit interactions on wave functions $\zeta(z,k_x,m_\mp)$ and spin components $S_j(z,k_x,m_\mp)$, we focus on the quantities $|\zeta_\alpha(z,k_x,m_\mp)|^2$ and $|\zeta_\beta(z,k_x,m_\mp)|^2$, which represent the probability density of measuring a $+z$-polarized and a $-z$-polarized spin, respectively, at a location z, for an electron in level $m_\mp$ having a wave vector k_x. Figure 3 shows these density distributions corresponding to $1L$ level computed with $k_x=0$ and various combinations of η_R, γ_D, and B. Examining Fig. 3, we observe the following.

(1) Increasing η_R (with $\gamma_D=0$ and $B=0.1$ T) results in increasing the spatial separation between the distributions $|\zeta_\alpha(z,k_x=0,1L)|^2$ and $|\zeta_\beta(z,k_x=0,1L)|^2$ along $\hat{z}$ [Fig. 3(a)]. For $\eta_R=0$, these distributions are superimposed on each other. This implies that the probability of measuring a net $\hat{z}$-polarized spin $[\Sigma_z(z,k_x=0,1L)=|\zeta_\alpha(z,k_x=0,1L)|^2 -|\zeta_\beta(z,k_x=0,1L)|^2]$ is zero everywhere along the width of the channel if spin-orbit interaction is absent. This is consistent with the fact that when $\eta_R=\gamma_D=0$ and $B\neq0$, all spins will be polarized in the direction of the external magnetic field, which is in the y direction. In that case, $S_y=1$ and $S_x=S_z=0$ everywhere. This is of course strictly true at 0 K temperature, which is what has been assumed here. With increasing η_R, we observe from Fig. 3(a) that the center of $|\zeta_\alpha(z,k_x,m_\mp)|^2$ moves toward one edge of the wire (i.e., $z=W_z$), whereas the center of $|\zeta_\beta(z,k_x,m_\mp)|^2$ moves toward the other edge ($z=0$). Thus, the Rashba effect creates a net $-z$ polarization (along $\hat{z}$) in the region $[0,W_z/2]$ (left half of the quantum wire) and a net $+z$ polarization in $[W_z/2,W_z]$ (right half of the quantum wire), so that S_z is negative in the region $[0,W_z/2]$ and positive in the region $[W_z/2,W_z]$ (see Fig. 4 later). This results in spin density modulation along the width of the wire, leading to spin texturing. We will show later that if the g factor of the material were positive instead of negative, then S_z would have been positive in the region $[0,W_z/2]$ and negative in the region $[W_z/2,W_z]$.

Since spins of opposite polarization accumulate at opposite edges of the wire in the presence of Rashba coupling, this is reminiscent of the intrinsic spin Hall effect (ISHE)[10,11] where similar spin accumulation takes place due to the Rashba effect. However, there are two differences. (1) In ISHE, the accumulated spins have polarizations along the y direction, whereas our accumulated spins have polarization along the z direction, and (2), the ISHE requires an electric field driving current along the axis of the wire, but here there is no such electric field. What we have instead is a magnetic field perpendicular to the wire axis (in the y direction). This magnetic field exerts a Lorentz force on the electrons so that electrons with negative velocity $-v_x$ are deflected to one edge and electrons with positive velocity $+v_x$ are deflected to the other edge of the wire (thus causing "edge states"). The Rashba interaction acts like an effective magnetic field B_R
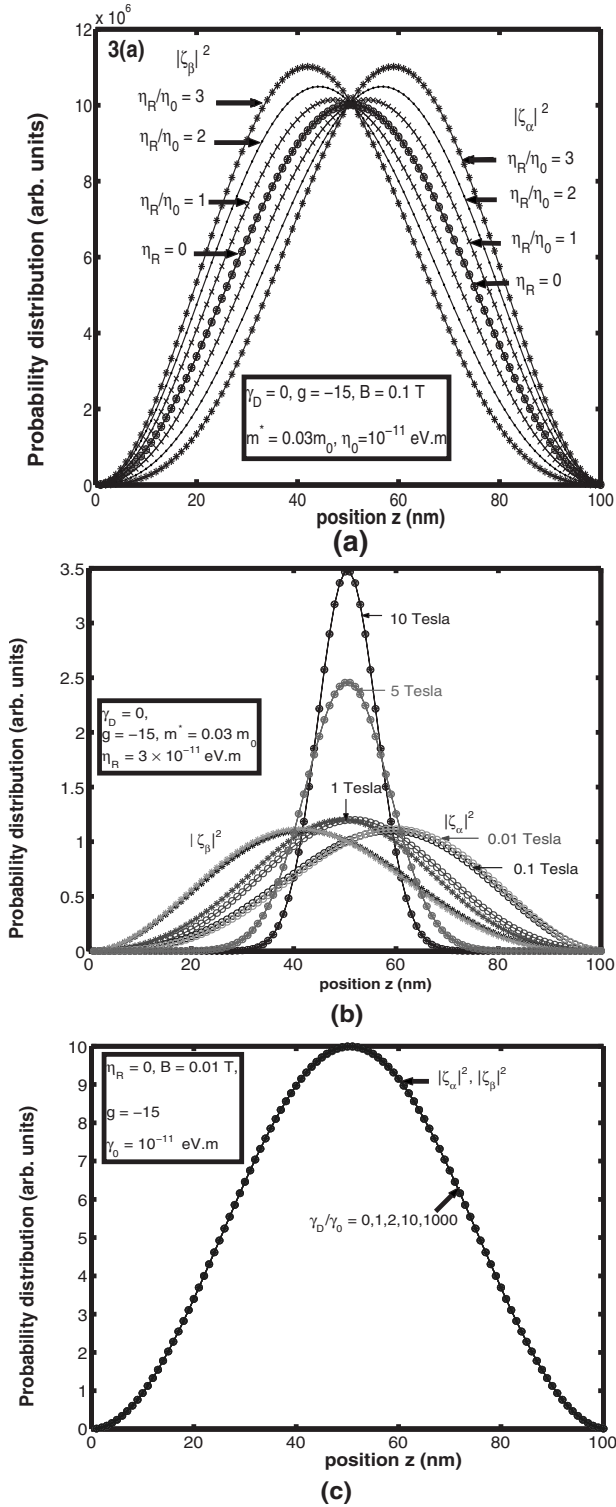
(a)

(b)

(c)

FIG. 3. Spatial distribution of $|\zeta_\alpha(z,k_x=0,1L)|^2$ and $|\zeta_\beta(z,k_x=0,1L)|^2$ for various combinations of η_R, γ_D, and B. (a) This plot shows that with increasing η_R (for fixed γ_D and B), $|\zeta_\alpha(z,k_x=0,1L)|^2$ is monotonically skewed toward $z=W_z$ and $|\zeta_\beta(z,k_x=0,1L)|^2$ toward $z=0$. The value of η_0 is 10^{-11} eV m. (b) The effect of B (for fixed η_R and γ_D) on $|\zeta_\alpha(z)|^2$ and $|\zeta_\beta(z)|^2$. With increasing B, these distributions come closer to each other. B is expressed in units of T. (c) The Dresselhaus constant γ_D has no effect on the shape of $|\zeta_\alpha(z)|^2$ and $|\zeta_\beta(z)|^2$. The value of γ_0 is 10^{-11} eV m. The material parameters of InAs have been used.
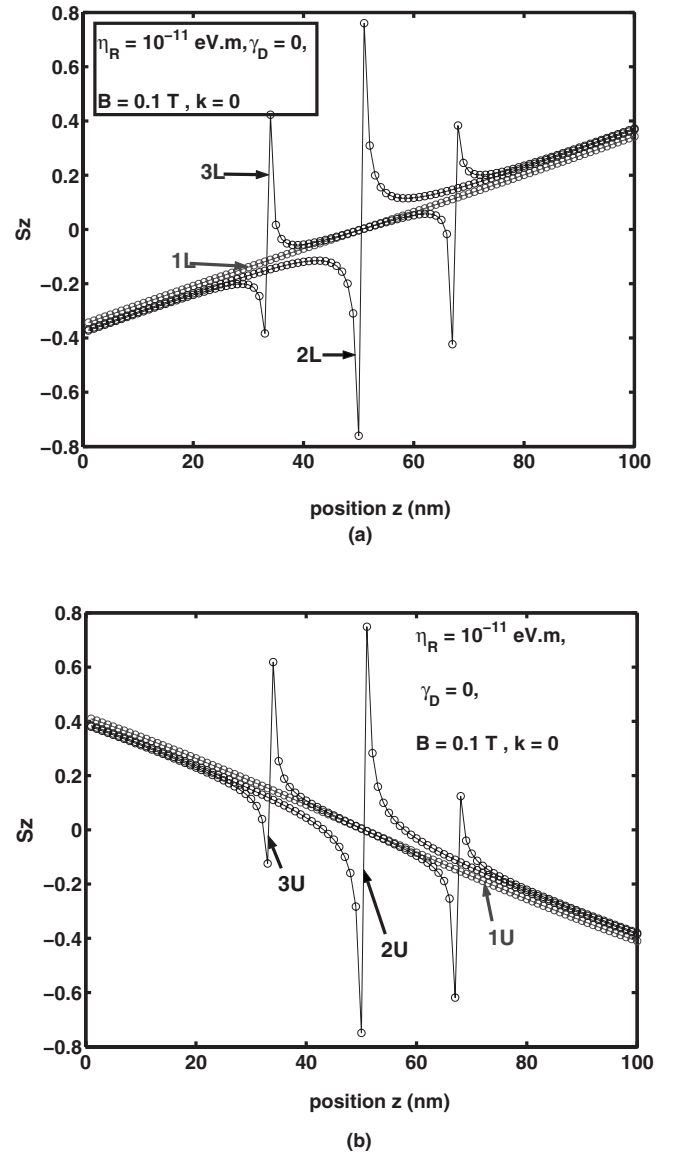

(a)

(b)

FIG. 4. Spatial variation of $S_z(z,k_x=0,m_\mp)$ for various subbands with $k_x=0$, $\gamma_D=0$, $B=0.1$ T, and $\eta_R=10^{-11}$ eV m. The spin densities are plotted for (a) the lower spin-split levels and (b) the upper spin-split levels in different subbands. Note that S_z exhibits discrete jumps wherever there is a node in the wave function. Also note that S_z is negative for $z<W_z/2$ and positive for $z>W_z/2$ for the $1L$ level, while the signs are reversed for the $1U$ level. The material parameters of InAs have been used. For a material with positive g factor, the behavior would be opposite (signs would be reversed).

whose magnitude is proportional to the magnitude of the electron velocity[12] and whose direction is along $v_x \times E_y$, i.e., along the $+z$ or $-z$ direction in this case. Since electrons with opposite velocities are localized at opposite edges of the wire, opposite edges experience oppositely directed B_R. Because spins will tend to align parallel to B_R (when the external field B is sufficiently weak), they assume antiparallel polarizations at the two edges (i.e., $+z$ polarized at one edge and $-z$ polarized at the other). This is the origin of the spin accumulation. We think of this effect as a *magnetostatic analog of the intrinsic spin Hall effect.* Note that the external

field B is needed for this effect to be manifested, since without it, the edge states will not form.

To understand the spin accumulation from a different perspective, consider the fact that the Rashba Hamiltonian involves a σ_z term [Eq. (2e)] which, for $k_x = q_x + eBW_z/2\hbar = 0$, has the form $H_R = (\eta_R eB/\hbar)(z - W_z/2)\sigma_z$. Equating H_R to $-g\mu_B \vec{B}_R \cdot \sigma$, which is the equivalent Zeeman interaction due to B_R, we immediately find that $B_R(z)$ is equal to $-(\eta_R eB)(z - W_z/2)/(\hbar g \mu_B)$. This field is zero at $z = W_z/2$, negative for $z < W_z/2$, and positive for $z > W_z/2$, if the g factor is *negative* (as in InAs). For materials with positive g factor, the signs will be opposite. For the 1L level, $\langle H_R \rangle$ must be minimum if we ignore the external field B, and this is achieved if spins are parallel to $B_R(z)$ at every z coordinate. Thus, we have $-\hat{z}$ spin polarization for $z < W_z/2$ and $+\hat{z}$ polarization for $z > W_z/2$ in a material with negative g factor. This, in turn, explains why $|\zeta_\alpha(z, k_x=0, 1L)|^2$ shifts toward $z = W_z$ and $|\zeta_\beta(z, k_x=0, 1L)|^2$ shifts toward $z = 0$ when $\eta_R \neq 0$.

In a material with positive g factor, the sign of B_R will be opposite. Hence, the sign of the spin polarization at any location z and the shifts will be opposite compared to a material with negative g factor.

From the above discussion, it also follows that for 1U level, $\hat{z}$ component of spin will be antiparallel to $B_R(z)$, implying that $|\zeta_\alpha(z, k_x=0, 1U)|^2$ and $|\zeta_\beta(z, k_x=0, 1U)|^2$ will shift toward $z=0$ and $z=W_z$, respectively, in a material with negative g factor. This is exactly what we observe (data not shown). Obviously, the shifts will be opposite for a material with positive g factor since B_R will have the opposite sign. The amount of shift for both 1L and 1U will increase with η_R since the Rashba interaction is responsible for the shift.

We have found that even for higher subbands mU and mL ($m > 1$), the effect of η_R is to spatially separate the peaks of $|\zeta_\alpha(z, k_x, m_\mp)|^2$ and $|\zeta_\beta(z, k_x, m_\mp)|^2$. For mL subbands, with increasing η_R, $|\zeta_\alpha(z, k_x, mL)|^2$ is skewed toward $z = W_z$ and $|\zeta_\beta(z, k_x, mL)|^2$ is skewed toward $z = 0$. For mU subbands, the effect is opposite, i.e., $|\zeta_\alpha(z, k_x, mU)|^2$ is increasingly skewed toward $z=0$ and $|\zeta_\beta(z, k_x, mU)|^2$ toward $z = W_z$ with increasing η_R. This is true for a material with negative g factor and the opposite behavior is observed when the g factor is positive, since the direction of B_R is reversed if the sign of the g factor is reversed. The spatial variation of $S_z(z, k_x, m_\mp)$ (i.e., the spin texturing effect) is, however, more complicated in higher subbands. The wave functions in the higher subbands have multiple nodes in the region $[0, W_z]$. Accordingly, $S_z(z, k_x, m_\mp)$ has multiple nodes along the z direction in the higher subbands. We show this in Fig. 4 for the case of $k_x = 0$ and $B = 0.1$ T.

The above description becomes more involved when $\gamma_D \neq 0$. Figure 5 shows the wave functions and spin components with finite γ_D. In this case, we have an additional z dependence of the effective spin-orbit magnetic field as should be evident from [Eq. (2e)].

(2) As we increase B (for fixed η_R and γ_D), the distributions $|\zeta_\alpha(z, k_x, m_\mp)|^2$ and $|\zeta_\beta(z, k_x, m_\mp)|^2$ are drawn closer to each other [Fig. 3(b)]. We can resolve the two distributions up to a flux density of ~ 1 T, after which they become indistinguishable from each other. This is consistent with the fact that the magnetic fields B_R and B_D, due to the two

types of spin-orbit interactions, become increasingly negligible compared to the external magnetic field B as the latter increases in strength. At very large B, we will have $S_y(z, k_x, m_\mp) \approx \mp 1$ and $S_x(z, k_x, m_\mp) \approx S_z(z, k_x, m_\mp) \approx 0$. Since $S_z(z, k_x, m_\mp) \propto (|\zeta_\alpha(z, k_x, m_\mp)|^2 - |\zeta_\beta(z, k_x, m_\mp)|^2)$, it is obvious that $|\zeta_\alpha(z, k_x, m_\mp)|^2 \approx |\zeta_\beta(z, k_x, m_\mp)|^2 \equiv |\zeta_0(z, k_x, m_\mp)|^2$, when B becomes very large. In this limiting case, one can write the total wave function as the product of a spatial part $\zeta_0(z)$ and eigenspinors of σ_y, i.e., $\zeta_0(z)[1, \pm i]^T$. The widths of the distributions also decrease with a corresponding increase in their heights as B increases in strength. At high B, electrons with small k_x form Landau orbits that will localize near the center of the wire with a narrow probability distribution. The radius of a Landau orbit is $\sqrt{h/eB}$, which decreases with increasing B, causing the distribution to become increasingly narrow with increasing B.

(3) Variation of Dresselhaus spin-orbit constant γ_D (for nonzero η_R and B) does not significantly affect the peak positions of $|\zeta_\alpha(z, k_x, m_\mp)|^2$ and $|\zeta_\beta(z, k_x, m_\mp)|^2$ [Fig. 3(c)]. Interestingly, if $\eta_R = 0$, γ_D by itself cannot shift the distributions. Only for finite η_R, the peaks of $|\zeta_\alpha(z, k_x, m_\mp)|^2$ and $|\zeta_\beta(z, k_x, m_\mp)|^2$ are shifted from each other along $\hat{z}$. This is easily understood. The Dresselhaus interaction acts like an effective magnetic field in the x direction, while the Rashba interaction acts like an effective magnetic field in the z direction. Thus, absent the Rashba interaction, the Dresselhaus interaction cannot affect $S_z(z, k_x, m_\mp)$, since it does not produce an effective magnetic field component in the z direction. Hence, it cannot, by itself, cause a nonzero $\Sigma_z(z, k_x, m_\mp) = |\zeta_\alpha(z, k_x, m_\mp)|^2 - |\zeta_\beta(z, k_x, m_\mp)|^2$, which would result in a net z polarization of spin and spatially separate $|\zeta_\alpha(z, k_x, m_\mp)|^2$ and $|\zeta_\alpha(z, k_x, m_\mp)|^2$ for a fixed k_x and $m_\mp$.

An interesting point to observe is that in the presence of spin-orbit interaction, the velocity of an electron is not proportional to momentum even if there were no external magnetic field. The relation between the two is *spin-dependent*. Note that the expectation value of $v_x^{op} = \partial H / \partial p_x$ (which is the operator representing the $\hat{x}$ component of velocity) takes the following form in the presence of spin-orbit interaction:

$$\langle v_x^{op} \rangle = \left\langle \frac{p_x + eBz}{m^*} \right\rangle + \frac{\eta_R}{\hbar}\langle S_z \rangle + (\gamma_D/\hbar)\langle S_x \rangle, \qquad (5)$$

where

$$\langle S_j \rangle = \int_0^{W_z} [\zeta_\alpha^*(z)\zeta_\beta^*(z)]\sigma_j[\zeta_\alpha(z)\zeta_\beta(z)]^T dz, \quad j = x, y, z.$$

Similarly, the expected value of $v_z^{op} = \partial H / \partial p_z$ is given by

$$\langle v_z^{op} \rangle = \left\langle \frac{p_z}{m^*} \right\rangle - \frac{\eta_R}{\hbar}\langle S_x \rangle - (\gamma_D/\hbar)\langle S_z \rangle. \qquad (6)$$

Figure 6 shows the dependence of each of the three terms on the right hand side of Eqs. (5) and (6) on the wave vector k_x for various values of the spin-orbit interaction strengths η_R and γ_D. Clearly, the quantities $(\eta_R/\hbar)\langle S_z \rangle$ and $(\gamma_D/\hbar)\langle S_x \rangle$ are not simply proportional to η_R and γ_D, respectively. The quantity $(\eta_R/\hbar)\langle S_z \rangle$ is affected by γ_D via the term $\sigma_z p_z$ in the Dresselhaus Hamiltonian and $(\gamma_D/\hbar)\langle S_x \rangle$ is affected by η_R
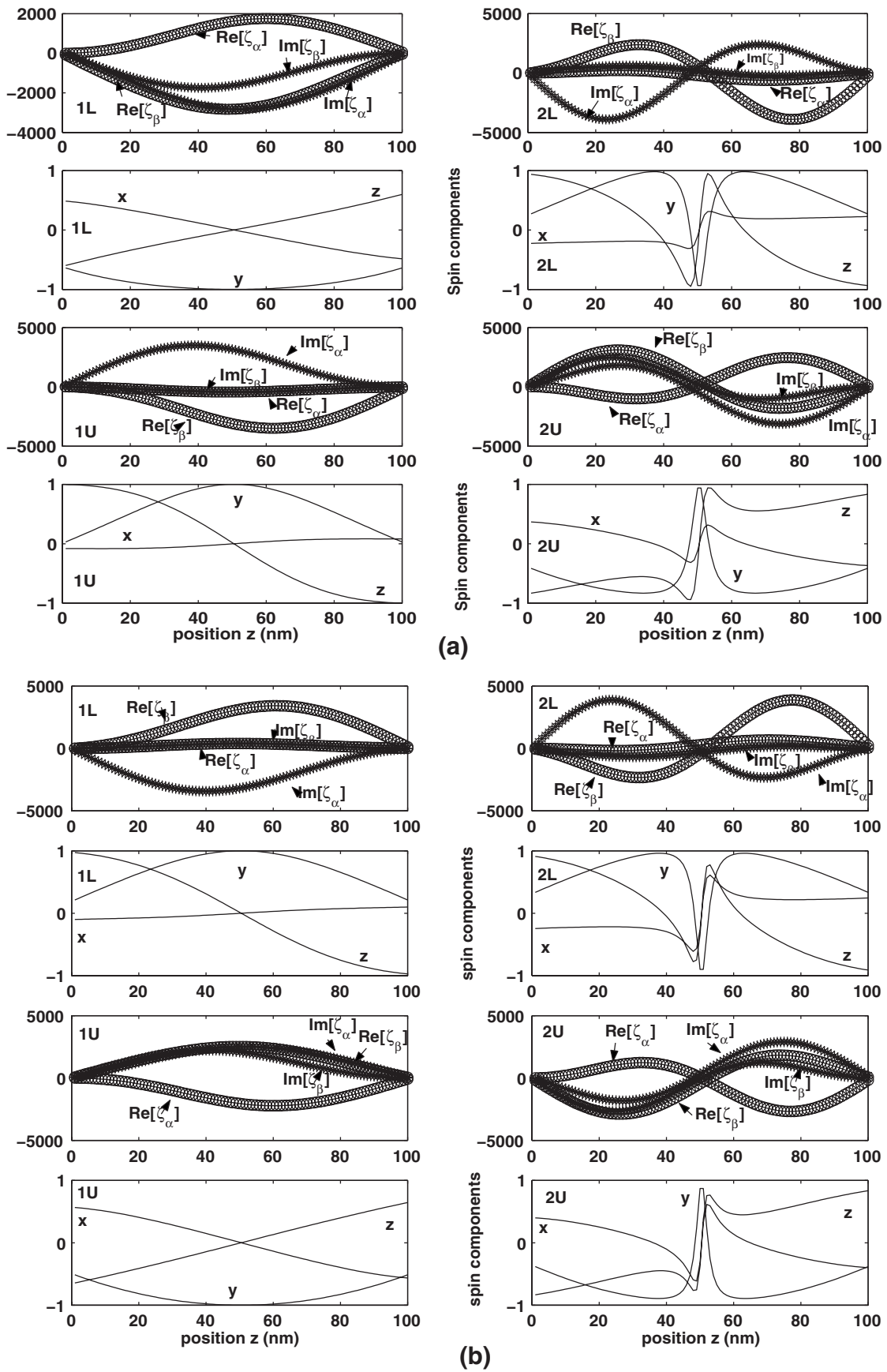
FIG. 5. Spatial variation of wave functions and spin components for 1L, 2L, 1U, and 2U levels with $k_x=0$, $\eta_R=3\times10^{-11}$ eV m, γ_D $=10^{-11}$ eV m, and $B=0.5$ T. The material parameters of InAs have been used: (a) $g=-15$ and (b) $g=+15$.
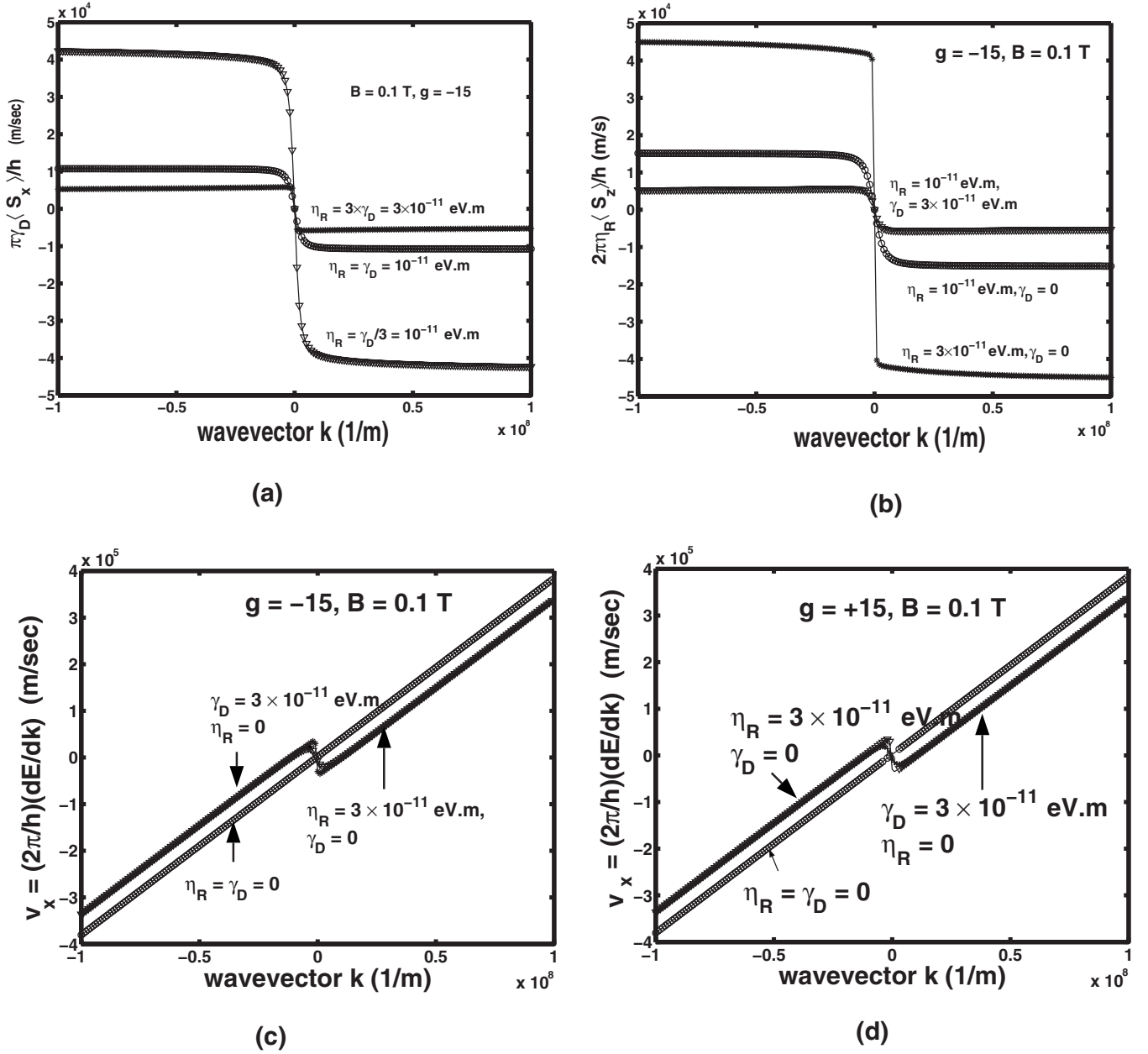
FIG. 6. Dependence of $\langle v_x \rangle$ and its components for the $1L$ state on wave vector k_x with various values of η_R, γ_D, and g. Magnetic field B is fixed at 0.1 T.

via the term $\sigma_x p_z$ in the Rashba Hamiltonian. Note from Fig. 6 that at $k_x=0$, all these components are individually equal to zero.

In Fig. 7, we plot Δ_z, which is the spatial separation between the peaks of the probability distributions $|\zeta_\alpha(z,k_x=0,m_\mp)|^2$ and $|\zeta_\beta(z,k_x=0,m_\mp)|^2$ along the z direction (width of the quantum wire), as a function of subband index m for both mL and mU levels. This quantity sublinearly increases with the subband index.

As mentioned earlier, in zeroth-order theory, the two-component spinor is written as the product of a spatial part and a spatially invariant spin part, i.e., $[\zeta_\alpha(z,k_x,m_\mp) \times \zeta_\beta(z,k_x,m_\mp)]^T = \psi(k_x,m,z)[\alpha_0(k_x,\mp)\beta_0(k_x,\mp)]^T$, where $\alpha_0(k_x,\mp)$ and $\beta_0(k_x,\mp)$ are z independent. Accordingly, an electronic state with a fixed k_x would appear to have

z-*independent* and m-*independent* spin orientation in every energy level. Moreover, these spin orientations should be antiparallel in the two spin-split levels of the same subband. In that case, we will expect that for an electron with a fixed k_x, the spin in $1L$ and mL ($m>1$) levels will be nearly parallel, whereas the spins in $1L$ and mU ($m \geq 1$) levels will be nearly antiparallel (they are not exactly parallel or antiparallel since the Dresselhaus interaction depends on the subband index m). In the absence of Dresselhaus interaction, electric dipole transitions would have been allowed only between $1L$ and mL levels, while being forbidden between $1L$ and mU levels.

In Fig. 8, we show that this expectation is belied if we go beyond the zeroth-order theory. The spatial distribution of the angle between the spin orientations in two spin-split levels of a subband, for $k_x=0$, is shown for various subbands as
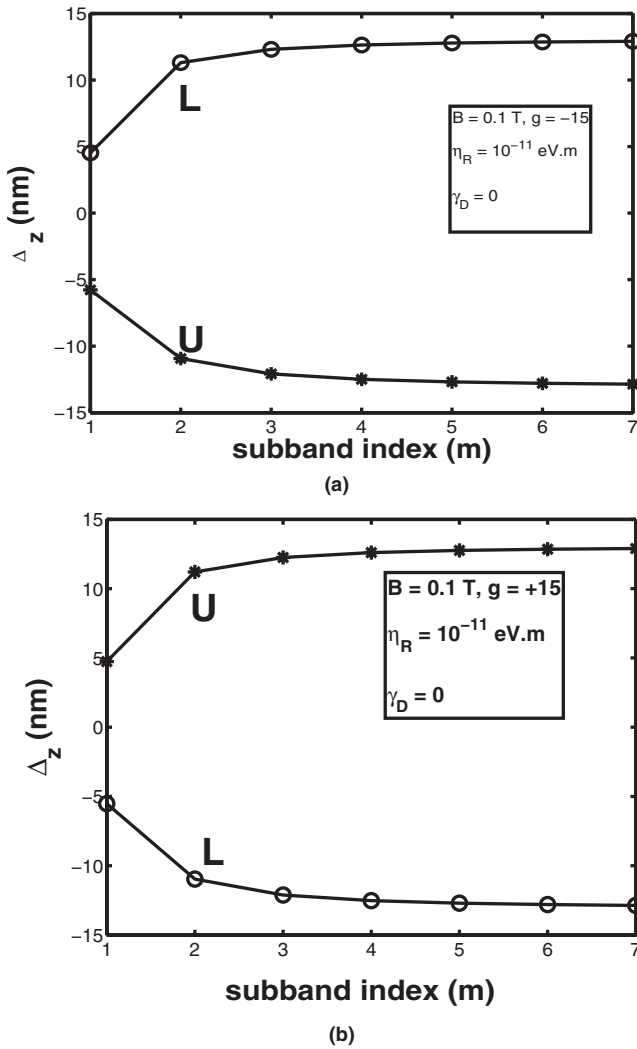
(a)

(b)

FIG. 7. The quantity Δ_z, which is the spatial separation (along the z axis) between the peaks of $|\zeta_\alpha(z)|^2$ and $|\zeta_\beta(z)|^2$, as a function of subband index m for $1L$ and $1U$ bands. The results are plotted for $B=0.1$ T, $\gamma_D=0$, and $\eta_R=10^{-11}$ eV m. (a) For InAs and (b) for a hypothetical material that has identical material parameters as InAs, except that the g factor is positive.

a function of z. It is clear from Fig. 8 that the spins belonging to two different spin-split levels with the same m and k_x are *not* antiparallel at every z coordinate. They are antiparallel only at the center of the wire (i.e., when $z=W_z/2$). Thus, the electric field component of an incident photon can couple the two spin-split levels in the same subband and induce electric dipole transitions between them, leading to strong absorption. This is in stark contrast to the observation made in Ref. 13 which states that such transitions can be mediated only by the magnetic field component of the incident photon (i.e., only the much weaker magnetic dipole transitions are allowed). This is understandable since Ref. 13 made the zeroth-order approximation, writing the wave function as a product of space-dependent and spin-dependent parts, which would immediately mask the possibility of electric dipole transitions between spin-split levels in the same subband. Thus, the zeroth-order approximation can lead to nontrivial errors in some cases.
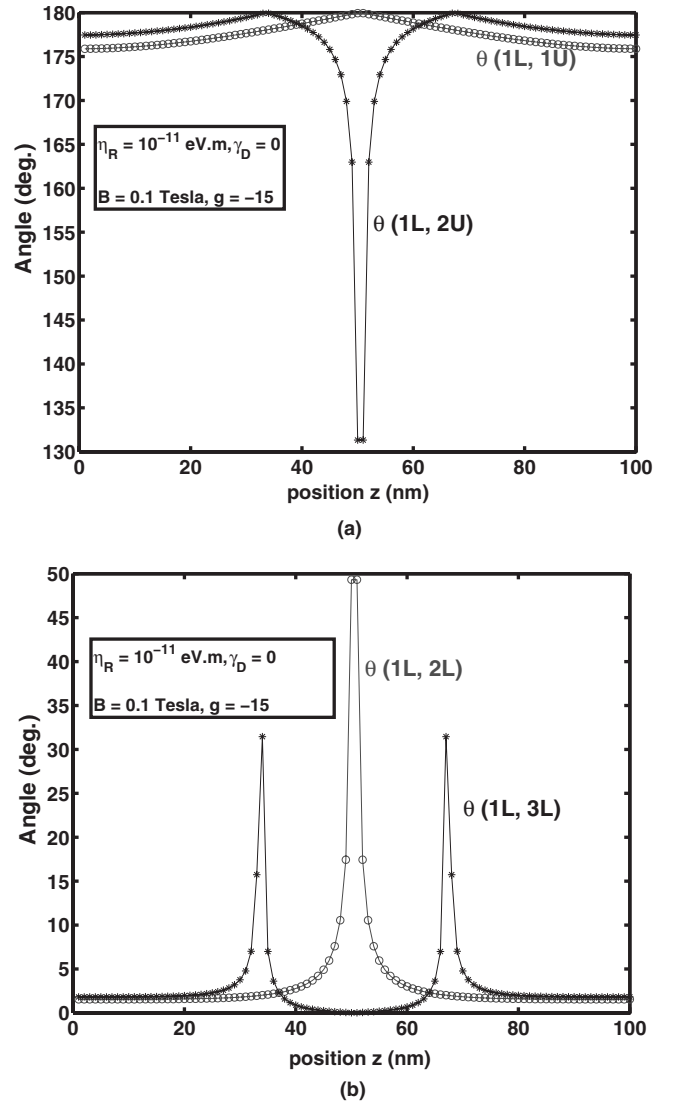

(a)

(b)

FIG. 8. Spatial distribution of the angles between the spin vectors belonging to different spin-split levels with $k_x=0$, $\eta_R=10^{-11}$ eV m, $\gamma_D=0$, and $B=0.1$ T. The area under each curve is a measure of the misalignment between the spins of two levels. The material parameters of InAs have been assumed. Note that iL and jL levels do not have parallel spins everywhere and iL and jU levels do not have antiparallel spins everywhere, either.

In an earlier work,[5] we have shown that the z dependent spin orientation makes the zone center ($k_x=0$) spin-splitting energy ($\Delta_{k_x=0}^m$) in any subband a function of the Rashba coupling strength (η_R) and the subband index m. This is now evident in Fig. 9, where we show the subband energies at $k_x=0$ in different subbands. The effects seen here (strong dependence of the spin-splitting energy in any subband on m and η_R) are not captured by the zeroth-order analytical solution of Eq. (2a) which yields (i) z independent S_j (no spin density modulation or spin texturing), (ii) antiparallel spin orientations of spin-split states with same m and k_x (thus no electric dipole transitions between them), and (iii) $\Delta_{k_x=0}^m=g\mu_B B$, independent of η_R and m.

The zone center ($k_x=0$) energies shown in Fig. 9 monotonically decrease with increasing Rashba spin-orbit cou-
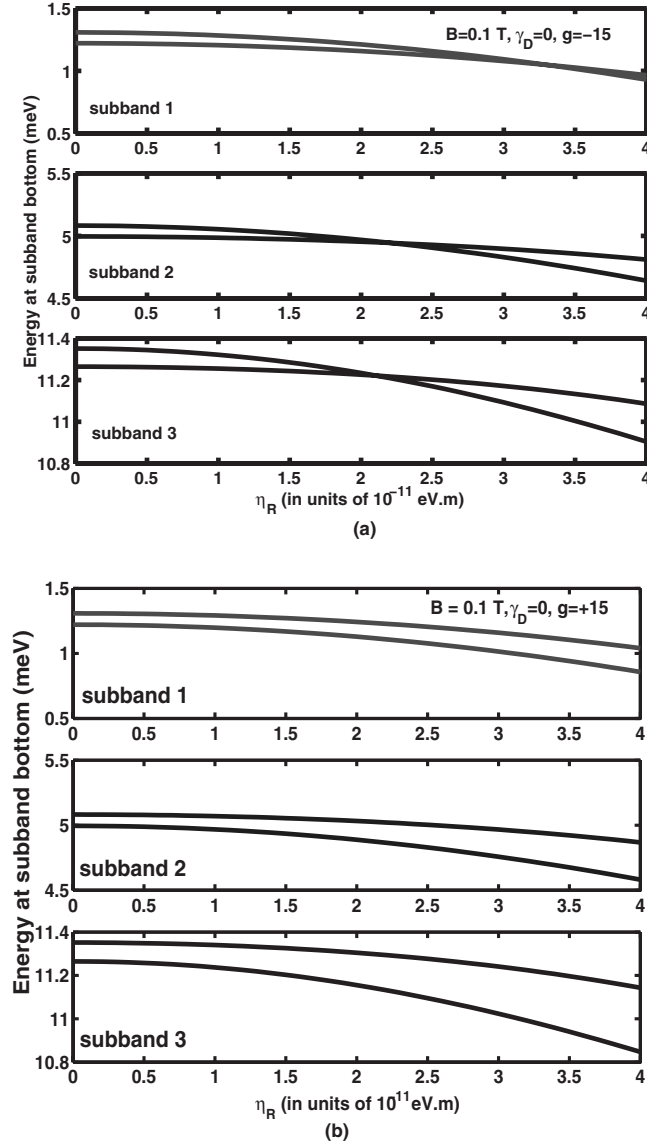
FIG. 9. Dependence of the energies of the spin-split levels in various subbands (at $k_x=0$) on the Rashba coupling strength η_R. Here, we have assumed that $B=0.1$ T and $\gamma_D=0$. (a) For InAs and (b) for a hypothetical material that has the same material parameters as InAs, except that the g factor is positive and equal to $+15$. Note that there are level crossings in a material with negative g factor, but not in a material with positive g factor.

pling strength η_R. The rate of decrease is always slower for the level whose spins tend to align antiparallel to the external magnetic field B compared to the level whose spins tend to align parallel. Thus, the mL level has a slower rate than the mU level when the g factor is negative, while the opposite is true when the g factor is positive. As a result, for a negative g-factor material, the energy splitting between mL and mU levels at first decreases with increasing η_R. Then there is a zero crossing where the levels become degenerate, and thereafter they switch so that the original mU level has lower energy than the mL level. This is a very interesting phenomenon since it suggests that the sign of spin polarization (i.e., the role of majority and minority spin) in any subband can be *reversed* by applying a sufficiently strong electric field E_y to

induce a sufficiently strong Rashba coupling. For a positive g-factor material, this feature is absent. The energy splitting between mL and mU levels continues to diverge with increasing η_R. There is no zero crossing and no switching of roles between majority and minority spins in any subband.

A. Photon induced transitions between subbands: Terahertz absorption

We now calculate the matrix elements for photon induced transitions between various energy levels and the intensity of absorption associated with such transitions. To do this, we replace $\vec{p}$ in the first term of Eq. (1) by $\vec{p}+eA_p(r,t)\hat{z}$, where $A_p(r,t)\hat{z}$ is the vector potential describing the electromagnetic field associated with the $\hat{z}$-polarized photon (in this work, we ignore any effect of the electromagnetic radiation on the spin state of the electrons). By using dipole approximation (small and r-independent A_p), we obtain the standard electron-photon interaction Hamiltonian[14–16]

$$H_{\text{e-p}} = \frac{eA_p\hat{z}}{2} \cdot \left[\frac{1}{m^*}\vec{p} + \vec{p}\frac{1}{m^*} \right] \equiv \frac{eA_p\hat{z}\cdot\vec{p}}{m}, \qquad (7)$$

assuming that the effective mass (m^*) is z independent. The intersubband transitions can be viewed as being caused by the perturbation term $(e/m^*)A_p\hat{z}\cdot\vec{p}$. Using Fermi's golden rule, the absorption intensity is given by

$$I = \Xi \left| \langle \zeta_i(z,k_x=0,\mu_{\mp})| \frac{d}{dz} |\zeta_f(z,k_x=0,\nu_{\mp})\rangle \right|^2, \qquad (8)$$

where $\zeta_i(z,k_x=0,\mu_{\mp})$ and $\zeta_f(z,k_x=0,\nu_{\mp})$ are the two-component wave functions of the initial and final states that have energies $E_i(k_x=0,\mu_{\mp})$ and $E_f(k_x=0,\nu_{\mp})$, such that $E_f(k_x=0,\nu_{\mp})-E_i(k_x=0,\mu_{\mp})=\hbar\omega$. Here, the subscripts i and f indicate the initial and final states, respectively, $\mu_{\mp}$ and $\nu_{\mp}$ are the initial and final levels, ω is the frequency of the absorbed photon, and Ξ is a proportionality constant. In this study, we fix the initial state to be $1L$. Intersubband transitions can be classified into two categories: (i) type I transitions which have the form $1L \rightarrow mL$ ($m=2,3,\ldots$) and (ii) type II transitions of the form $1L \rightarrow mU$ ($m=1,2,3,\ldots$). Type I transitions are the normally allowed ones and type II transitions would have been forbidden by the zeroth-order theory. We call them the "normally forbidden" transitions.

Figure 10 shows absorption intensity (I) for transitions between various spin-split levels in an external magnetic flux density of 0.1 T for InAs ($g=-15$) and a hypothetical material that has identical parameters as InAs, except that $g=+15$. These transitions are caused by the electric field component of the incident photon. The magnetic field component is, in general, several orders of magnitude weaker than the electric field component and hence has been ignored in the present study. Note that the maximum intensity occurs for the $1L \rightarrow 2L$ transition. This can be understood from Fig. 8, which shows that the average misalignment angle (proportional to the area under the curves in Fig. 8) is lowest between $1L$ and $2L$, so that this transition has the largest matrix element and the strongest intensity.
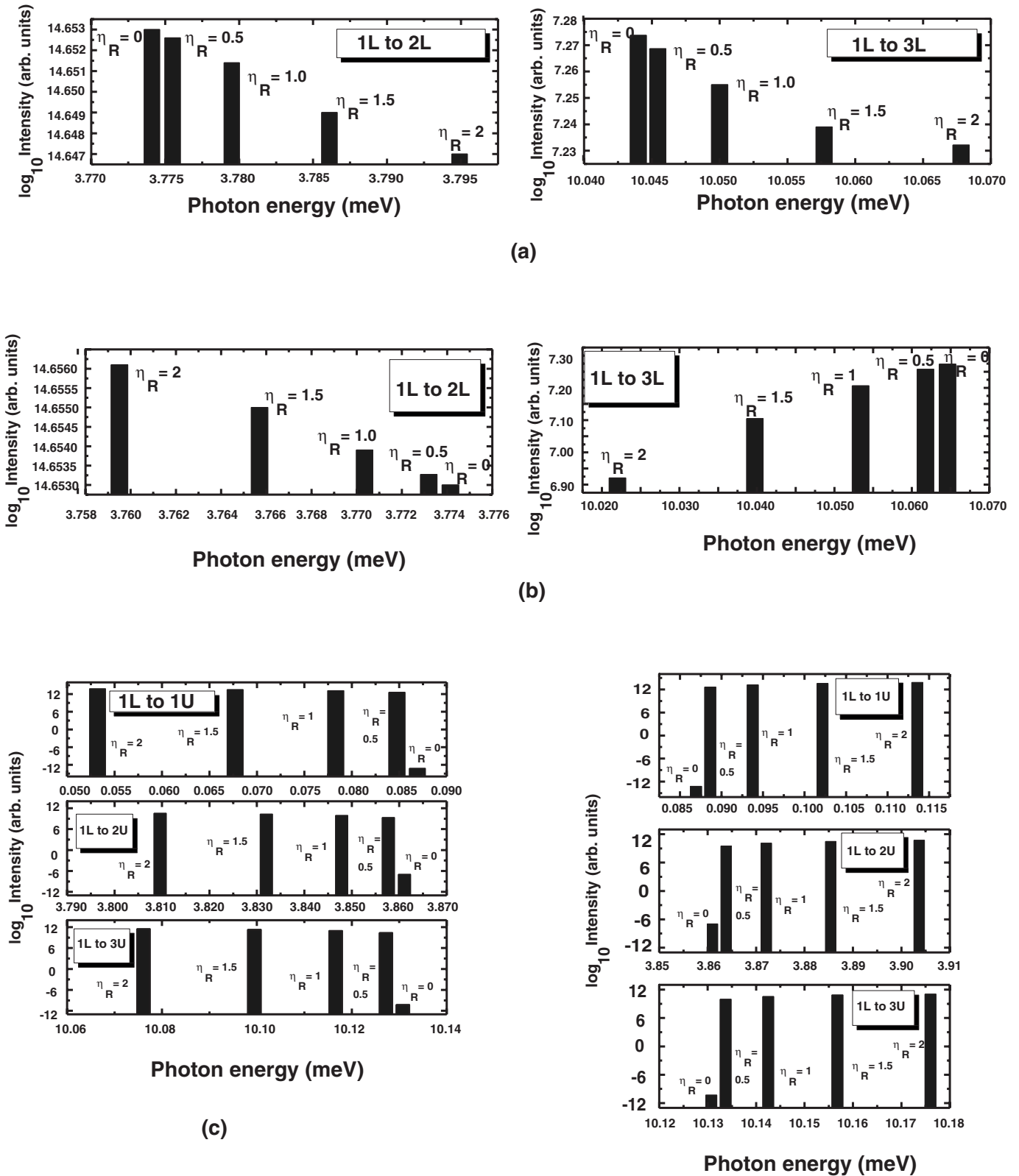
FIG. 10. Absorption intensity versus absorbed photon energy, as a function of Rashba coupling strength η_R. (a) Type I transitions for InAs (intensity slowly decreases with increasing Rashba coupling, which is accompanied by a blueshift), (b) type I transitions for a hypothetical material with the same material parameters as InAs, except that the g factor$=+15$ (intensity either slowly increases or decreases with increasing Rashba coupling, which is accompanied by a redshift), (c) type II transitions for InAs (intensity rapidly increases at first and then levels off, with an accompanying redshift), and (d) type II transitions for a hypothetical material that has the same parameters as InAs, except that the g factor$=+15$ (intensity rapidly increases at first and then levels off, with an accompanying blueshift).

For type I transitions in a material with negative g factor, the absorption intensity slowly decreases with increasing Rashba coupling η_R with an accompanying blueshift in the position of the absorption peak. The amount of blueshift slowly increases with subband index m. This can be understood from Fig. 9(a) which shows that the photon energy absorbed for a given type I transition slowly increases with increasing η_R and the amount of increase becomes slightly more pronounced if the final state is in a higher subband. In a material with positive g factor, the behavior is more complicated. The absorption intensity of type I transitions slowly increases with increasing Rashba coupling strength for the $1L$ to $2L$ transition, but slowly decreases for the $1L$ to the $3L$ transition. There is always a redshift in the position of the absorption peak. The amount of redshift slowly increases with subband index m. The redshift can be understood from the energy diagrams in Fig. 9(b).

In the case of type II transitions in a material with negative g factor, the absorption intensity at first increases much more rapidly with Rashba coupling strength compared to type I transitions (in fact, it increases by 24 orders of magnitude as the Rashba coupling increases from 0 to 5 $\times 10^{-12}$ eV m), but then begins to level off. The position of the peak is, however, redshifted with increasing η_R. Again, this can be understood from Fig. 9(a) which shows the dependence of the energy of the absorbed photon on η_R. In a material with positive g factor, the absorption intensity again rapidly increases with increasing η_R and then begins to level off. However, the position of the peak is blueshifted. Also note that for small values of η_R, $I(1L \rightarrow mL) \gg I(1L \rightarrow mU)$, where I is the absorption intensity. This merely implies lower transition probability between approximately opposite spin states (with large spin misalignment angle) and larger probability of transition between similarly oriented spin states. With increasing η_R, the overall misalignment between the spins is somewhat reduced, making them less antiparallel. This explains the rapid increase in intensity of type II absorption with increasing η_R.

Figure 10 clearly shows that we can modulate the absorption intensity with an electric field which controls the Rashba spin-orbit coupling strength. The absorption intensity will decrease for type I transitions and increase for type II transitions, with increasing electric field, regardless of whether the g factor is positive or negative. This leads to *amplitude modulation*. We can also shift the position of the peak frequency with the electric field. A blueshift is obtained for type I transitions in a material with negative g factor or type II transitions in a material with positive g factor, whereas a redshift is obtained for type II transitions in a material with negative g factor or type I transitions in a material with positive g factor. This leads to *frequency modulation*. In Fig. 11, we show the absorption peaks associated with both type I and type II transitions, as a function of the Rashba spin-orbit coupling strength, in a hypothetical material that has the same parameters as InAs, except that the g factor is +4. Figure 11 makes it obvious that both amplitude and frequency modulation are achievable.

Note that the photon energies in Fig. 10 correspond to meV energies that imply terahertz radiation. The ability to modulate both the frequency and strength of terahertz absorption with an external electric field allows one to fabricate different detectors, detecting slightly different terahertz frequencies, on the same wafer. Each detector is a quantum wire with a gate and different gate potentials are applied to different wires to make them detect slightly different frequencies. This results in a *multispectral* terahertz detector. The system is reconfigurable since we can change the detection frequencies at will by changing the gate potentials.

A photoexcited electron relaxes to the ground state by emitting photons (photoluminescence). The frequency of the emitted photon depends on the level separation in energy between initial and final states and the intensity of emission depends on the matrix element coupling these states. Based on the preceding discussion, it is clear that both the frequency and intensity can be changed with a gate voltage, resulting in an amplitude or frequency modulator. In modulator applications, the carrier signal will be the emitted light and the modulating signal will be the one applied to the gate of the quantum wire. Thus, we can implement terahertz frequency and/or amplitude modulators by modulating the spin-orbit interaction strength in a quantum wire with a gate voltage.
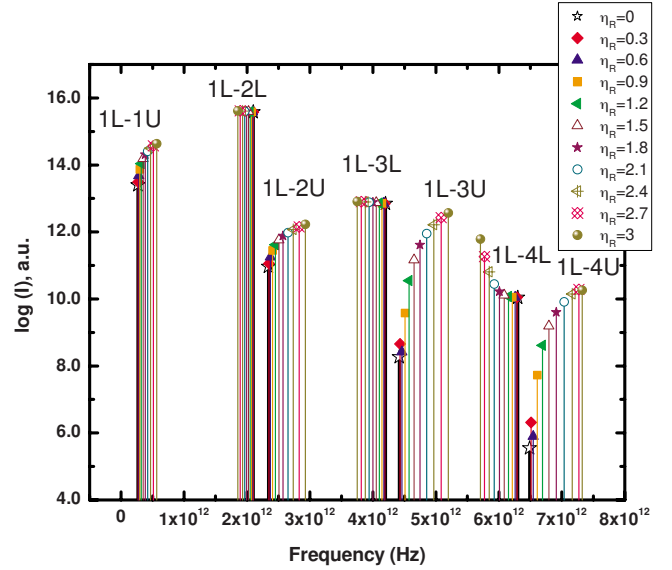

FIG. 11. (Color online) Absorption intensity as a function of photon frequency for various Rashba coupling strengths. We have assumed a hypothetical material with effective mass$=0.067m_0$ and g factor$=+4$. This figure clearly illustrates the nature of amplitude and frequency modulation achievable with a gate potential that varies the Rashba coupling strength.

IV. CONCLUSION

In this paper, we have presented an exact calculation of the magnetoelectric subbands and the two-component spinor wave functions in a quantum wire in the presence of Rashba and Dresselhaus spin-orbit interactions. We have shown that these quantities can be varied by varying the strength of the Rashba interaction with a gate potential. Physical models have been presented to explain these results. We have also

calculated the photon induced intersubband transition probabilities and showed that electric dipole transitions deemed forbidden according to zeroth-order theory are actually allowed since spin vectors in spin-split levels of the same sub-band are not antiparallel everywhere. We have shown that it is possible to control the absorption intensity and frequency by electrostatic means. This could lead to reconfigurable multispectral terahertz detectors and modulators.

[1] Y. Bychkov and E. Rashba, J. Phys. C **17**, 6039 (1984).

[2] G. Dresselhaus, Phys. Rev. **100**, 580 (1955).

[3] J. A. Nesteroff, Y. V. Pershin, and V. Privman, Phys. Rev. Lett. **93**, 126601 (2004).

[4] J. A. Nesteroff, Y. V. Pershin, and V. Privman, IEEE Trans. Nanotechnol. **4**, 141 (2005).

[5] S. Pramanik, S. Bandyopadhyay, and M. Cahay, Phys. Rev. B **76**, 155325 (2007).

[6] C. W. J. Beenakker and H. van Houten, in *Solid State Physics*, Semiconductor Heterostructures and Nanostructures Vol. 44, edited by F. Seitz and D. Turnbull (Academic, San Diego, 1991), pp. 1–228.

[7] S. Chaudhuri and S. Bandyopadhyay, J. Appl. Phys. **71**, 3027 (1992).

[8] P. Upadhyaya, S. Pramanik, S. Bandyopadhyay, and M. Cahay, Phys. Rev. B **77**, 045306 (2008).

[9] M. Governale and U. Zülicke, Phys. Rev. B **66**, 073311 (2002).

[10] J. Inoue and H. Ohno, Science **309**, 2004 (2005).

[11] J. Sinova, D. Culcer, Q. Niu, N. A. Sinitsyn, T. Jungwirth, and A. H. MacDonald, Phys. Rev. Lett. **92**, 126603 (2004).

[12] L. Meier, G. Salis, I. Shorubalko, E. Gini, S. Schön, and K. Ensslin, Nat. Phys. **3**, 650 (2007).

[13] Y. V. Pershin and C. Piermarocchi, Appl. Phys. Lett. **86**, 212107 (2005).

[14] S. Datta, *Quantum Phenomena*, Modular Series on Solid State Devices (Addison-Wesley, New York, 1989), Chap. 7.

[15] Ph. Lelong, S.-W. Lee, K. Hirakawa, and H. Sakaki, Physica E (Amsterdam) **7**, 174 (2000).

[16] R. Q. Yang, Phys. Rev. B **52**, 11958 (1995).